

## *Progress on the theory of orographic precipitation*

Ronald B. Smith<sup>\*</sup>

*Department of Geology and Geophysics, Yale University, New Haven, Connecticut 06520, USA*

### ABSTRACT

**This paper presents a review of recent progress on the theory of orographic precipitation and a discussion of the role of preexisting atmospheric disturbances, especially their strong water vapor fluxes. I also introduce the basic elements of stable moist airflow dynamics and cloud physics, and a new linear theory of orographic precipitation. The theory is tested against two types of data: a single event of Alpine precipitation and the annual climatology of the Oregon coastal ranges. Different methods are used to determine the free “cloud-delay” parameters in the theory, including a statistical analysis of data from conventional rain gauges and isotope analysis of stream samples. The surprising threshold behavior of nonlinear accretion-dominated cloud physics is displayed. Finally, I consider the impact of scale-dependent precipitation patterns on erosion and terrain evolution.**

**Keywords:** mountains, rain, orographic precipitation, clouds.

### 1. INTRODUCTION

While the influence of terrain on precipitation is widely appreciated, the explanations of the processes involved are often oversimplified. One inaccurate assertion is that mountains can produce precipitation by themselves, acting in normal “climatological” circumstances. This idea is mostly, but not entirely, untrue. Mountains have their most profound influence on precipitation during brief events when significant pre-existing atmospheric disturbances move into mountainous areas. In other words, mountains usually modify, and often amplify, rather than create precipitation. Here are a few examples on both sides of this issue.

First, consider two examples of orographic precipitation that do not require a preexisting disturbance. On the eastern slopes of Hawaii’s Big Island, facing the easterly trade winds, bands of precipitation form daily in the summer and move onshore, triggered in part by the airflow blocking effect of the high volcanic mountains (Wang et al., 2000). Four thousand miles to the east, in the summertime Rocky Mountains in Colorado, daily solar heating of the mountain slopes induces thermal updrafts that evolve into precipitating thunderstorms by mid-afternoon (Raymond and Wilkening, 1982; Banta and Barker Schaaf, 1987). These predict-

able daily occurrences suggest that these mountains require only average seasonal conditions to generate precipitation.

Mountains can also act systematically to suppress precipitation. In regions with steady prevailing winds, the leeward slopes of mountain ranges usually experience descending air in which clouds or precipitation cannot occur. Solar heating effects can also suppress cloud formation. An example is the Mesopotamian valley of Iraq, adjacent to the high Iranian Plateau. In the summer, solar heating of the plateau generates a circulation with a descending air over Mesopotamia, preventing cloud formation and precipitation there (Evans et al., 2004).

The influence of mountains in modifying precipitation from preexisting weather disturbances is very widespread and found in all climate zones. In mid-latitude, cool-season climates, precipitation is generally controlled by the “weather cycle,” i.e., the quasi-periodic passing of frontal cyclones. With intervals from 4 to 7 d, these cyclones produce precipitation wherever they occur, but the patterns and amount of precipitation can be strongly modulated by terrain. For example, Pacific Ocean cyclones crossing the mountainous western coast of North America produce copious rainfall events generating floods and landslides. As the cyclones move into the intermountain west and the Rocky Mountains, they produce deep snowfalls that generate mountain glaciers

<sup>\*</sup>E-mail: ronald.smith@yale.edu.

and avalanches (Rauber and Grant, 1986). Between these brief storm events, little precipitation occurs. Later in the spring, when warm-weather episodes melt the mountain snowpack, bursts of river discharge cause further erosion and landscape alteration.

Analogous events can be found in other mid-latitude regions. Nor'easters approaching New England from the south bring strong, moist, easterly airflows over the White and Green Mountains, the Adirondacks, Berkshires, and Catskills. The precipitation patterns are strongly modified by these hills (Passarelli and Boehme, 1983). In Europe, cyclones passing north of the Alps bring snowfall to the northern slopes, while cyclones passing along the Mediterranean Sea bring heavy rains to the southern Alpine slopes. The average or "prevailing" westerly winds have little to do with these events (Buzzi et al., 1998).

Consider now the dry subtropics. Under average conditions in these latitudes, descending air in the Hadley Cell prevents cloud formation. Precipitation is rare. The prevailing dryness is spectacularly reversed when a hurricane forms. When a drifting hurricane hits high terrain, the patterns of precipitation in the cyclone are profoundly altered. Without such disturbances, the mountains produce little precipitation.

A region with frequent hurricanes (i.e., typhoon) impacting high terrain is Taiwan. There, typhoons usually approach from the east (Lin et al., 1999). If the storm center passes south of the Central Mountain Range, the counterclockwise typhoon circulation creates easterlies that hit the eastern slopes. Severe rain

rates, flooding, and landslides will occur there (Fig. 1). On the western (lee side) slopes, the air descent is so strong that the air will dry and clouds will disappear. Surprisingly, so intense is the local orographic downslope effect that a dry foehn can exist inside the typhoon.

On other occasions, the typhoon center may pass north of the Central Mountain Range. As the storm with its cyclonic winds moves away toward the west, strong westerlies hit the Central Mountain Range with rain on the western slopes and dry eastern slopes.

In the cool seasons, Taiwan can be impacted by frontal cyclones as well. During the January 2003 GSA Penrose Conference in Taiwan, a strong winter frontal system hit the island while the attendees drove from west to east across the Central Mountain Range. Heavy rain changed to snow as they ascended the mountain roads. Beyond the ridgeline, the skies cleared. A view back toward the west showed the classic foehn wall cloud over the crest, marking the beginning of dry descent. These interesting meteorological events captured the attention of the rock hammer-wielding geologists briefly before they returned to their investigations of faults, metamorphic grades and landforms, seeking clues to the long-term effects of such recurring weather events.

Like Taiwan, the massive Himalayan front in Asia experiences precipitation events in both seasons. In the summer, the monsoon onset vortex brings heavy rains to the foothills of the

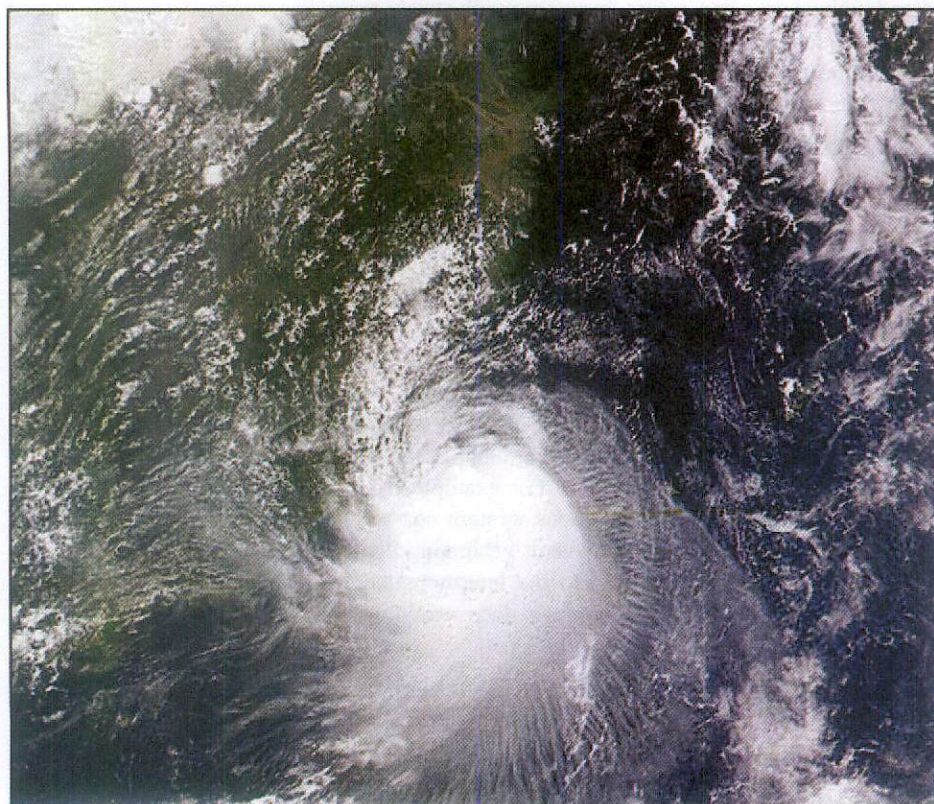


Figure 1. Typhoon Toraji over Taiwan on 30 July 2001. This three-band false-color satellite image is from the SeaWiFS sensor (courtesy of National Aeronautics and Space Administration [NASA]). Taiwan is obscured by high clouds, but the coast of China is evident. This storm caused several deaths, numerous landslides, and rapid erosion on the steep slopes of the Central Mountain Range.



Himalayas, while the high Tibetan Plateau is mostly dry (Barros and Lang, 2003). In winter, frontal storms push snow further up into the high terrain.

The dominance of disturbances can also be illustrated in the Southern Hemisphere. Both the New Zealand Southern Alps (Wratt et al., 1996) and the southern Andes lie squarely in the belt of eastward-drifting frontal cyclones. The wet-dry contrast across both ranges is marked, but the precipitation on the windward slopes is intermittent, not continuous. The precipitation events on these ranges are not responding directly to the average prevailing winds, so much as to the impact of discrete moist frontal cyclones.

Even in Antarctica, it is the frontal cyclones translating eastward along the coast that produces moist northerly airflows, carrying water vapor up over the ice sheet where it condenses and precipitates. The orographic lifting enhances the lifting already present in the cyclone to increase the total precipitation rate. The climatological mean winds tell us little about these processes. At low levels, the mean flows near the Antarctic coast are southerly (i.e., downslope), as katabatic winds blow off the continent.

To summarize the connection between meteorological disturbances and orographic precipitation, we should focus on how these disturbances temporarily alter the regional environment. A critical factor is the enhanced horizontal water vapor flux in strong moist winds. As discussed later, orographic precipitation is roughly proportional to the horizontal water vapor flux. The sensitivity to wind speed is amplified by the fact that strong moist winds are better able to climb over high mountains, instead of flowing around. Also important is the increased relative humidity in fronts and cyclones, reducing the amount of lifting needed to produce condensation. Finally, the preexisting rain or snow in an atmospheric disturbance may improve the efficiency with which new orographically generated condensate is converted to precipitation.

The role of weather disturbances in orographic precipitation has implications in climate and terrain reconstructions over geologic time. It implies that wet and dry climates depend on storm tracks more than on mean flows and that brief rain events rather than continuous rains usually control climate, vegetation, and landform processes.

In the following sections, I discuss several key issues in the theory of orographic precipitation. Additional background information can be found in reviews by Smith (1979), Banta (1990), and Barros and Lettenmaier (1994).

## 2. MOIST AIRFLOW DYNAMICS

The basic thermodynamics of orographic precipitation is firmly established. As air is forced to rise over sloping terrain, the air parcels expand and cool. As the air temperature drops, the relative humidity increases and eventually water vapor must condense. Usually, the condensation occurs on numerous dust particles to form small cloud droplets. After the conversion of cloud droplets to larger hydrometeors (i.e., rain or snow), these par-

ticles fall under the influence of gravity to form precipitation (Wallace and Hobbs, 1977).

The starting point for the analysis of orographic precipitation is the study of moist airflow dynamics and the realization that the nature of the terrain-induced ascent depends on the width ( $a$ ) of the hill (e.g., Smith, 1979). For narrow hills (i.e.,  $a < 1$  km), the vertical penetration ( $z$ ) of the forced ascent is limited to about  $z = a$ . For wider hills, two other factors enter the airflow problem: density stratification and latent heat release.

A measure of the effect of density stratification is the stability frequency ( $N$ ) given by

$$N^2 = \frac{g}{T} [\gamma - \Gamma], \quad (1)$$

where  $g$  is acceleration due to gravity,  $\gamma$  and  $\Gamma$  are the actual and adiabatic lapse rates, respectively. Under typical tropospheric conditions  $\gamma = -0.0065$  °C/m,  $\Gamma = -0.0098$  °C/m and  $T = 273$  K, so  $N \sim 0.01$  s<sup>-1</sup>. The natural buoyant oscillation period of the air is  $T = 2\pi/N \approx 600$  s = 10 min. With air parcels wanting to return to their initial altitude within ten minutes, simple ascent forced by sloping terrain is converted into a more complex gravity wave. Mountain-generated gravity waves have been extensively studied over the past 50 yr (e.g., Smith, 1979; Wurtele et al., 1996). Gravity wave flow fields are characterized by upwind tilting patterns of airflow disturbances, such as those shown in Figure 2. The strength and penetration depth of the forced vertical motion is limited by the phase tilt in these waves. The approximate penetration depth of the vertical motion, for simple hydrostatic flow, is

$$z = U/N. \quad (2)$$

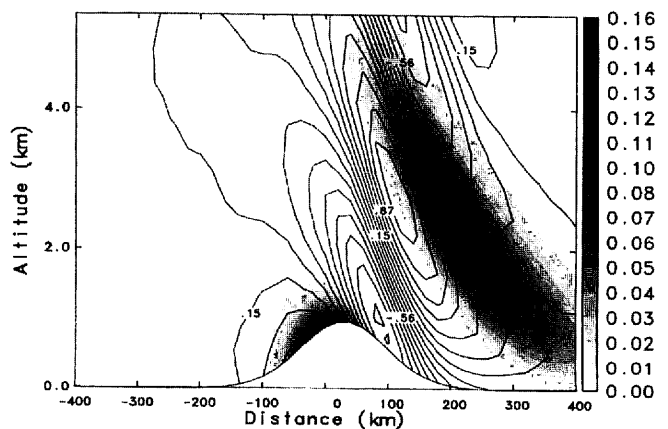


Figure 2. Vertical cross section of moist airflow over an idealized mountain shape. The control parameters are: stability  $N = 0.011$  s<sup>-1</sup>, wind speed  $U = 10$  ms<sup>-1</sup>, mountain width  $a = 10$  km, mountain height  $h_m = 1000$  m. Airflow is from left to right. The field of vertical velocity is contoured with an interval of 0.086 m/s. The snow mixing ratio is shaded with interval 0.01 g/kg. Note the upwind tilted patterns and the limited vertical penetration of the forced ascent above the windward slope. (Image is from Jiang and Smith, 2003.)

Using wind and stability values,  $U = 10$  m/s and  $N = 0.01$  s<sup>-1</sup>, this penetration height is  $\sim 1000$  m. Air passing over the hill above that level (say at 2000 m) will not feel the terrain forced ascent, or may even descend in the mountain-generated gravity wave (Fig. 2).

For very high terrain, the approaching flow may be decelerated and forced to split and flow around the mountain. This can profoundly reduce the amount of forced ascent. The accepted condition for flow splitting uses scaling laws based on the ambient flow speed ( $U$ ), the stability frequency ( $N$ ), and the mountain height ( $h$ ). Roughly, if the nondimensional mountain height

$$M = hN/U > 1, \quad (3)$$

the air will tend to flow around rather than over the hill. For  $U = 10$  m/s and  $N = 0.01$  s<sup>-1</sup>, hills higher than 1 km will exceed this limit and flow splitting will result. The approach to stagnation and flow splitting for a circular Gaussian hill is shown in Figure 3. As  $M$  increases toward the critical value ( $M = 1.3$  in this case), the minimum wind speed in the windward region drops to zero. Beyond  $M = 1.3$ , the low-level flow splits and flows around the hill.

The above estimates neglect the effect of latent heat release caused by water vapor condensation during ascent. It has been suggested by several authors that the flow splitting condition (equation 3) might still apply if the adiabatic lapse rate  $\Gamma$  was replaced by the moist adiabatic lapse rate  $\Gamma_m$ , and the dry stability frequency  $N$  is replaced by  $N_m$ , the moist stability frequency (e.g., Durran and Klemp, 1982; Barcilon and Fitzjarrald, 1985). Typical values of  $N_m$  are significantly less than  $N$ , often only one-half to one-third as large (e.g.,  $N_m \sim 0.005$  s<sup>-1</sup>). This substitution in

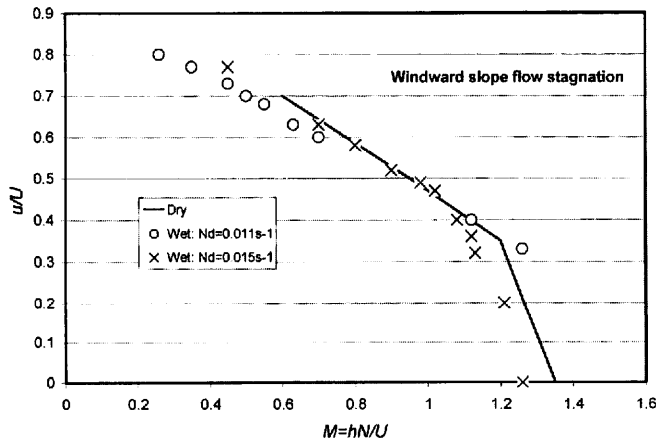


Figure 3. This diagram shows how the wind upstream of a mountain is decelerated depending on the nondimensional mountain height ( $M$ ). The deceleration ratio,  $(u/U)$  was determined from a full three-dimensional nonlinear numerical model of airflow dynamics. The solid curve is for a dry atmosphere. The two sets of symbols repeat the calculation for a moisture-saturated atmosphere. The results collapse to a single curve when  $M$  is computed with the moist stability frequency. (Data are from Jiang, 2003.)

equation 3 predicts that moist air could rise over hills two or three times as high as dry airflow could. And, using the example above, the penetration of forced ascent could increase to 2 or 3 km. If the depth of the moist layer is  $H_w = 3$  km, the deeper penetration of forced ascent will catch a much bigger fraction of the moisture flux across the terrain.

The validity of the moist stability substitution has been most carefully studied by Jiang (2003) in the context of orographic precipitation. Jiang showed that the onset of flow nonlinearity and flow splitting could be predicted by equation 3 with  $N$  replaced by  $N_m$  (Fig. 3). The figure shows the onset of stagnation for dry airflow, and two cases of saturated airflow with different dry stabilities. The critical value of  $M = 1.3$  is maintained.

Jiang also showed that substantial regions of dry lee-side descent would occur, but that they did not seriously impact the use of moist stability in flow field computations for the upwind region. This confirmation opens up the possibility of analytic treatments of airflow associated with orographic precipitation (see section 4) without the patching of wet-dry regions proposed by Barcilon and Fitzjarrald (1985).

The influence of latent heating on airflow can take another form when the mountains are high. According to Doyle and Smith (2003), latent heating over a relatively small depth can tune the atmosphere for a nonlinear resonance that leads to strong descent in the lee. This result may solve the old conundrum of how air, heated by water vapor condensation, can be forced to descend on the lee slopes causing foehn.

### 3. CONDENSED WATER ADVECTION, CONVERSION, FALLOUT, AND EVAPORATION

The second key element in the physics of orographic precipitation is the behavior of the various categories of condensed water. The small cloud droplets, formed by vapor condensation in rising air, will be carried downwind by the ambient flow while undergoing a conversion to larger particles or "hydrometeors" (Uttal et al., 1988; Yau and Rogers, 1989; Yuter and Houze, 2003). Hydrometeors are defined as particles large enough that they have a significant terminal fall speed under the influence of gravity. A typical hydrometeor (i.e., a raindrop or snowflake) has a mass a million times greater than a cloud droplet, so the conversion is a nontrivial step in the formation of precipitation. Current estimates of the time ( $\tau_c$ ) necessary for conversion range from 200 to 2000 s, depending on a wide variety of physical factors, such as temperature, aerosol content, and turbulence.

Once hydrometeors have formed, they fall to the ground with their terminal velocities ( $V_t$ ). An estimate of  $V_t = 2$  m/s is appropriate for snow, while  $V_t = 6$  m/s is appropriate for rain. The fallout time ( $\tau_f$ ) depends also on the height from which hydrometeors must fall ( $H$ ) according to  $\tau_f = H/V_t$ . With cloud heights varying from 1 to 5 km, values of  $\tau_f$  can vary widely from 166 s to 2500 s. Colder conditions, with snow, will favor the larger values. Often in mid-latitudes the temperature profile will favor snow aloft, but rain at the surface. The falling snowflakes will

melt when they reach the 0 °C level and accelerate to a faster terminal speed.

These conversion and fallout time scales are of primary importance, because the lifting caused by terrain is temporary. After air crosses the ridgeline, descent dominates. Any condensed water that has not converted and precipitated before descent begins is subject to evaporation. A quantitative example can illustrate the point. Consider a ridge with half-width of  $a = 10$  km in a wind of  $U = 10$  m/s. Under these conditions, the time it takes a parcel to travel from the foothill to the crestline is  $T = a/U = 1000$  s. With a cloud-delay time of  $\tau_c = \tau_f = 200$  s, the conversion and fallout would have been well completed before descent begins. Conversely, if  $\tau_c = \tau_f = 2000$  s, only a small fraction of the condensed water could precipitate. The rest of the condensed water will evaporate on the lee side and return to the vapor state.

The cloud-delay processes also control the amount of precipitation that spills over onto the lee slopes. Lee slope precipitation is significant because it falls into a different watershed than the windward slope precipitation. A few kilometers of downwind shift in precipitation can be amplified to hundreds of kilometers by the terrain-controlled river network.

Certainly the best way to appreciate the role of cloud time scales is to observe a lenticular cloud; one of the most beautiful sights in nature (Fig. 4). In the lenticular cloud, orographic lifting condenses vapor to form cloud droplets or tiny ice crystals, but there is insufficient time for conversion. When the air descends, the warming air evaporates the condensate according to reversible thermodynamics. No precipitation occurs. The air mass has not been dried. Note that the image in Figure 4 can be reversed left to right without changing its basic nature, suggesting this thermodynamic reversibility.

As a prototype physical model of cloud physics, I consider the pair of steady-state condensate advection equations proposed by Smith (2003). The horizontal advection of vertically integrated condensed water is written as

$$\vec{U} \cdot \nabla q_c = S(x, y) - q_c / \tau_c, \quad (4a)$$

$$\vec{U} \cdot \nabla q_f = q_c / \tau_c - q_f / \tau_f, \quad (4b)$$

where  $\tau_c$  and  $\tau_f$  are the characteristic time scales for cloud water conversion and hydrometeor fallout. The term  $S$  in 4a is the source term, defined as the rate at which supersaturated water vapor is generated by ascent. When  $S$  is positive, I assume that the excess vapor is immediately condensed to form small cloud droplets. The cloud water and hydrometeor column densities ( $q_c, q_f$ ) have units of  $\text{kg m}^{-2}$ . The rate of conversion of cloud water to hydrometeor ( $q_c / \tau_c$ ) is assumed to be proportional to the cloud water column density with a rate coefficient of  $\tau_c^{-1}$ . The precipitation term in equation 4b [ $P(x, y) = q_f / \tau_f$ ] is proportional to the hydrometeor column density with a rate coefficient of  $\tau_f^{-1}$ . I assume that the cloud parameters  $\tau_c$  and  $\tau_f$  are constant throughout the region. The symbol  $\vec{U}$  is the regionally averaged horizontal wind vector, with eastward and northward components  $U$  and  $V$ . The

vector product of the wind and gradient vectors can be written in Cartesian form  $\vec{U} \cdot \nabla q = U \partial q / \partial x + V \partial q / \partial y$ .

A simple form for the condensed water source term was proposed by Smith (1979):

$$S(x, y) = \rho q_s \vec{U} \cdot \nabla h(x, y), \quad (5)$$

under the assumptions that the vertical air motion is independent of height, the air is saturated with vapor, and the temperature sounding follows a saturated moist adiabat. The factors  $\rho$  and  $q_s$  are the air density and specific humidity at Earth's surface. According to equation 5, the condensation rate is proportional to the terrain slope and wind speed. This model is referred to as the raw upslope model, if it is also assumed that conversion and fallout are instantaneous ( $\tau_c = \tau_f = 0$ ) so that equation 4 gives  $P(x, y) = S(x, y)$ .

In equation 4, as forced ascent drives  $S$  positive, the amount of cloud water increases downwind. The conversion term in equation 4 then acts to decrease cloud water and generate rain water. The precipitation term in equation 4b is the final sink to the system.  $S$  is negative in downslope regions. Persistent negative  $S$  can evaporate cloud water and rain water created upwind and prevent further precipitation.

One special solution of equation 4 can be found by noting that the advection term on the left-hand side scales like  $q / \tau_a$ , where the advection time scale is  $\tau_a = a / U$  and  $a$  is the characteristic mountain width. If the cloud conversion is slow (i.e.,  $\tau_c \gg \tau_a$ ), equations 4 and 5 give  $q_c(x, y) = \rho q_s h(x, y)$  and  $q_f = 0$ , indicating that the column integrated cloud water is proportional to the mountain height at each point; perhaps illustrated by the lenticular cloud in Figure 4.

#### 4. A LINEAR THEORY OF OROGRAPHIC PRECIPITATION

Several theories of orographic precipitation have been proposed, starting with the early work of Hobbs et al. (1973), Fraser et al. (1973), and Collier (1975). A brief review of existing theories is given by Barstad and Smith (2005). I focus here on the recent linear theory of orographic precipitation by Smith and Barstad (2004). It has several good properties. It (1) is analytically tractable, so that its properties can be easily understood; (2) is applicable to actual complex terrain and arbitrary wind direction, so that it can be tested against real data; (3) reduces to the classical upslope model in equation 5, so that it can be compared with earlier work; (4) includes the basic physical elements: air-flow dynamics, condensed water conversion, advection and fallout, and downslope evaporation, leading to a theory of precipitation efficiency; but (5) is limited to modest mountain heights so that  $M \ll 1$  (equation 3) and drying ratio  $DR \ll 1$  (see below).

Smith and Barstad (2004) pointed out that the airflow dynamics equations (not shown here) and cloud physics equations 4a and 4b can be solved together using Fourier transforms to obtain a single formula relating terrain and precipitation



photo by jane english (www.eheart.com)

Figure 4. Lenticular cloud over Mount Shasta in California. The photo was taken in February 1995 looking northeast over Lake Siskiyou. Note the left-to-right reversible aspect of the image. Photo by Jane English (www.eheart.com).

$$\hat{P}(k, l) = \frac{C_w i \sigma \hat{h}(k, l)}{[1 - i m H_w][1 + i \sigma \tau_c][1 + i \sigma \tau_f]}, \quad (6)$$

with vertical wavenumber

$$m(k, l) = \left\{ \left[ \frac{N_m^2 - \sigma^2}{\sigma^2} \right] (k^2 + l^2) \right\}^{1/2},$$

and then

$$P(x, y) = \iint \hat{P}(k, l) e^{i(kx + ly)} dk dl + P_\infty. \quad (7)$$

Equation 6 is a transfer function relating the Fourier transforms of the terrain  $h(k, l)$  and the precipitation field  $\hat{P}(k, l)$ . The spatial field of precipitation  $P(x, y)$  can be recovered with the inverse Fourier transform in equation 7. The symbols in equations 6 and 7 are described in Table 1. The first bracket in the denominator in equation 6 describes how the source term is modified by airflow dynamics. In this factor, the vertical wavenumber  $[m(k, l)]$  controls the depth and tilt of the forced air ascent. The two remaining brackets in equation 6 describe the advection of condensed water during conversion and fallout. The model reduces to the raw upslope model when  $H_w = \tau_c = \tau_f = 0$  and the uplift sensitivity factor  $C_w = \rho q_v$ . Downwind of steep lee slopes, if negative values arise in equation 7, they are truncated with  $P = \max(P, 0)$ . If the background precipitation  $P_\infty$  is sufficiently large, and the terrain is small, the truncation is not needed.

TABLE 1. SYMBOLS USED IN THE LINEAR MODEL

Name	Symbol	Typical values
Terrain elevation	$h(x, y)$	1–2000 m
Horizontal wavenumbers	$k, l$	0.001–0.0000001 $\text{m}^{-1}$
Intrinsic frequency	$\sigma = U/k + V/l$	0.01–0.0001 $\text{s}^{-1}$
Horizontal wind components	$U, V$	1–50 m/s
Moist stability frequency	$N_m$	0–0.01 $\text{s}^{-1}$
Water vapor scale height	$H_w$	1–5 km
Conversion time	$\tau_c$	200–2000 s
Fallout time	$\tau_f$	200–2000 s
Uplift sensitivity factor	$C_w$	0.001–0.02 $\text{kgm}^{-3}$
Background precipitation rate	$P_\infty$	0–5 mm/h
Vertical wavenumber	$m(k, l)$	0.01–0.0001 $\text{m}^{-1}$

Note: From Smith and Barstad (2004).

Note that the dynamics and cloud-delay factors in the denominator of equation 6 have a similar form. The appearance of  $i = \sqrt{-1}$  in each factor causes a phase shift of the pattern relative to equation 5, in addition to the amplitude change. The opposite sign in the dynamic and cloud factors is significant. The negative sign in the dynamics factor gives an upwind shift to the precipitation pattern, while the positive signs in the cloud factors cause a downwind shift (see also section 8). These factors also

differ significantly in the way that horizontal wavenumber ( $k, l$ ) enters the formulae for vertical wavenumber  $m(k, l)$  and intrinsic frequency  $\sigma(k, l)$ . Note that the two cloud time scales,  $\tau_c$  and  $\tau_r$  are mathematically analogous.

The properties of the linear model are illustrated in Figure 5 by evaluating it for moist airflow over a triangular ridge with a height of 500 m. Due to the uniform slopes of the triangle ridge, the raw upslope model (equation 5) gives a condensation rate that is constant from ridge base to peak. If this condensed water fell instantly to the ground, the precipitation rate would be 16 mm/hr. On the lee slope, the source function ( $S$ ) is negative.

When stratified airflow dynamics is included, the condensation pattern is shifted upstream, and its area integral is reduced. Its maximum value of 12 mm/hr occurs near the slope break  $\sim 15$  km upstream of the crest. When cloud-delay effects are included, the precipitation pattern is shifted downwind. The maximum precipitation rate (3 mm/hr) occurs in the vicinity of the ridge crest. The near coincidence of maximum precipitation and maximum terrain elevation is often seen in nature. Here it arises from a 7 km upwind shift from wave tilt and a 15 km downwind shift due to cloud delays. The cloud delay significantly decreases the total precipitation as cloud droplets and hydrometeors are advected past the crestline to evaporate over the lee slopes.

The efficiency with which vapor can be rained out is a function of mountain scale, as discussed in section 3. The scale dependence of condensation and precipitation is shown in Figure 6. The condensation efficiency is the ratio of source  $S$  to the raw upslope value (equation 6). The precipitation efficiency is the ratio of precipitation ( $P$ ) to condensation source ( $S$ ). As the scale increases, the vertical motion penetrates more deeply into the atmosphere, increasing the condensation efficiency. Also, as scale increases, more condensed water is able to convert and fall

out before being carried to the lee-side region of descent, increasing the precipitation efficiency. Further aspects of the theory are given by Smith and Barstad (2004).

The linear model is easy to apply to real terrain. Required only are the terrain height array  $h(x, y)$  and the parameters describing the atmospheric conditions (Table 1). The terrain is transformed, equation 6 is applied, and the inverse transform is computed (equation 7). Two examples are given in Figure 7, based on a 1-km-resolution terrain array. Using the Fast Fourier Transform algorithm, only a few seconds are required to generate these fields on a computer workstation. Both examples, the Olympics in Washington State and the eastern Mediterranean coastal ranges, have terrain with multiple scales. Cloud delays of  $\tau_c = \tau_r = 1000$  s were used for both examples.

In the Olympics, a smooth pattern of precipitation begins upwind over the sea. Near the terrain, the pattern responds to the four ridges that verge toward the southwest. The upwind-facing valleys between them receive much less precipitation. The lee slopes in the northeast are dry.

In the Levant, the first mountain range receives heavy precipitation while the second gets much less. Near  $33^\circ\text{N}$ , where the first range is much lower, the second range receives more precipitation. The shielding of the leeward by the windward range is surprising, considering that the linear model does not have a complete water vapor budget. If the ranges were separated much more widely, the linear model would predict identical precipitation amounts. The predicted precipitation patterns in these two regions have not yet been compared with rain gauge data.

## 5. AN ALPINE PRECIPITATION EVENT

One way to study orographic precipitation is to examine particular events (e.g., Browning et al., 1974). The study of special cases works well if the environmental parameters, such as

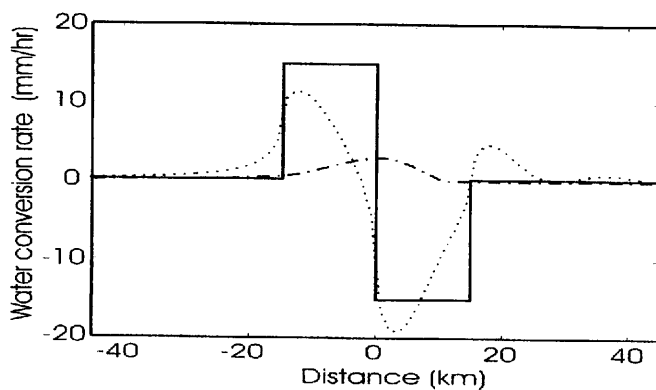


Figure 5. Precipitation rates (mm/h) over a triangle ridge with three different assumptions: solid—precipitation patterns with no airflow dynamics or cloud delays (equation 5), dotted—dynamics only, dashed—dynamics and cloud delays (equations 6 and 7). Parameters are:  $a = 15$  km,  $U = 15$  m/s,  $N_m = 0.005$  s $^{-1}$ ,  $T_0 = 280$  K,  $H_m = 2500$  m,  $\tau_c = \tau_r = 100$  s,  $A = 500$  m,  $P_\infty = 0$ . Airflow is from left to right. Note the great reduction in total precipitation caused by airflow dynamics and cloud delays. (Data are from Smith and Barstad, 2004.)

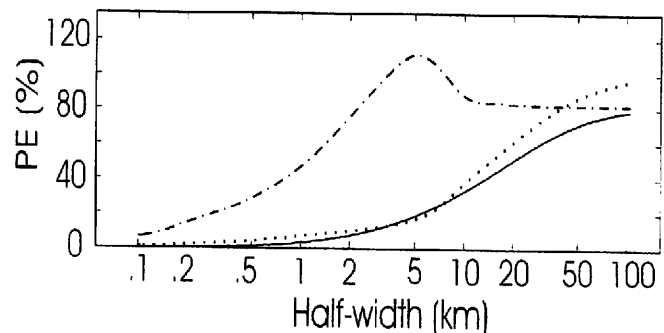


Figure 6. Three efficiency ratios (PE = precipitation efficiency) are plotted as a function of mountain half-width for a Gaussian ridge according to the linear model (equation 6). The condensation efficiency (dashed) is the ratio of the condensation to the raw upslope model (equation 5). The precipitation efficiency (dotted) is the ratio of the precipitation to the condensation. The solid curve is the ratio of precipitation to the raw upslope prediction. (Data are from Smith and Barstad, 2004.)

temperature, lapse rate, wind speed and direction, and background precipitation, can be accurately determined. Also, in real complex terrain, the predicted precipitation fields are highly structured in space and time. Therefore, a dense rain gauge network is required to validate the predicted patterns.

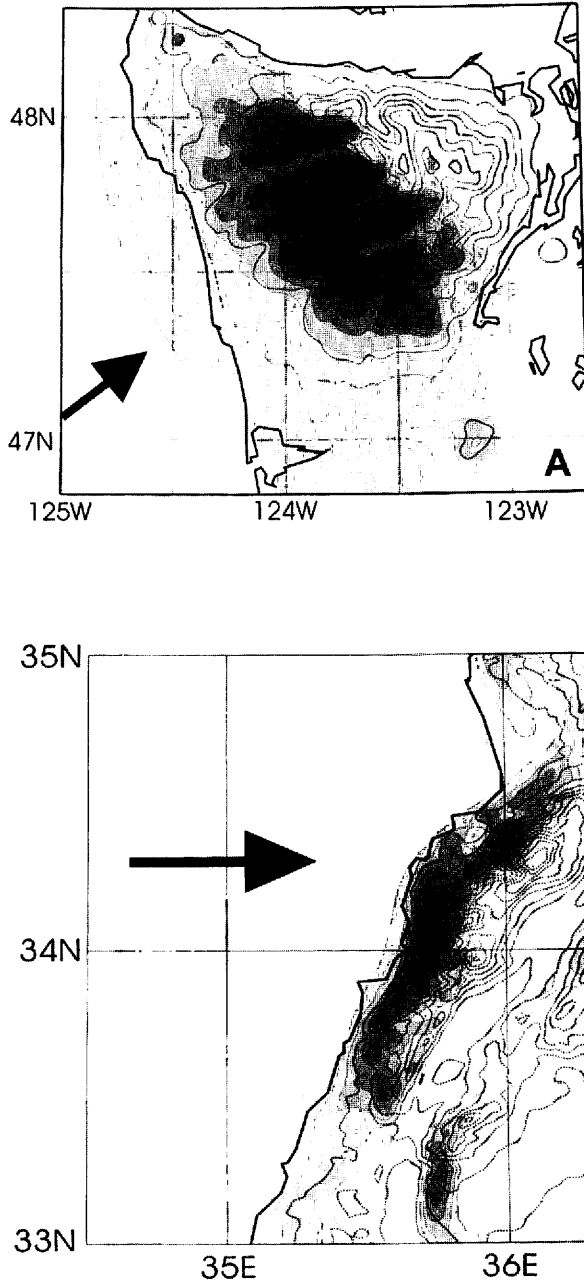


Figure 7. Two real-world applications of the linear model (6, 7): (A) the Olympic Mountains of Washington State (from Smith and Barstad, 2004) and (B) the Mediterranean coastal ranges of Lebanon and Israel. The 6 h accumulated precipitation is shown shaded with a 2.5 mm contour interval. The maximum precipitation is  $\sim 25$  mm in both cases. The terrain is shown (dotted) with a 200 m contour interval. The coastline is shown with a dark solid line. Large black arrows show the wind direction.

Without any doubt, the most intensely studied event of orographic precipitation in the history of meteorology was the 20 September 1999 Lago Maggiore event during the Mesoscale Alpine Programme (MAP) field phase (Georgis et al., 2003; Bousquet and Smull, 2003; Asencio et al. 2003; Medina and Houze, 2003; Smith et al., 2003; Doyle and Smith, 2003; Rotunno and Ferretti, 2003; Smith, 2003). Readers wishing to compare different scientific approaches to the same natural event have an ideal opportunity here.

The 20 September event was caused by a frontal cyclone transiting Spain, producing an 18 h period of moist southerly airflow against the southern slopes of the Alps (Fig. 8). Using the best available full numerical weather prediction models (COAMPS, MC2, and ECMWF), the water vapor influx and precipitation field were deduced (Smith et al., 2003). These models provide an optimum interpolation between radiosonde stations. The incoming flux of water vapor is illustrated in Figure 9. This figure shows that the depth of the moist layer is  $\sim 3$  km and that  $\sim 2.5$  km of lifting must occur if the flow is to cross over the Alpine ridge crest. The two models (COAMPS and MC2) roughly agree in their estimates of incoming flux, adding confidence to the result.

These flux fields were integrated to obtain estimates of the total water budget over a 24 h period (Table 2). The models estimated that  $\sim 50 \times 10^{11}$  kg of water vapor entered Box A (Fig. 8) from the south. The model estimates of precipitation were less

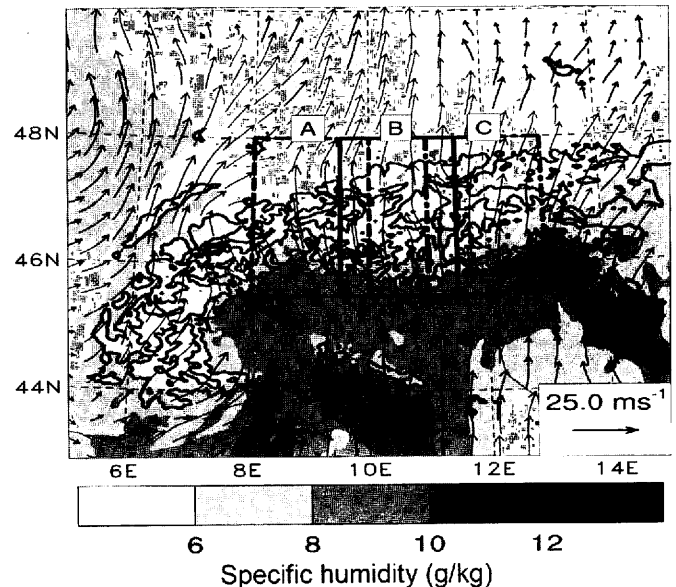


Figure 8. Planform view of Alpine flow at 06 UTC 20 September 1999, showing the COAMPS low-level specific humidity (g/kg) and wind fields at 50 m above ground level. Also shown are the boxes A, B, and C used in budget analyses. Strong moist southerly flow approached the Italian Alps. The dry area in the northeast is caused by the drying action of the Alps. (Data are from Smith et al., 2003.)



certain. They varied from 19 to  $12 \times 10^{11}$  kg. The rain gauge observations suggest that the former value is the correct one. The model differences primarily arose from different parameterizations of cloud physics processes. The drying ratio for Box A,

$$DR = \text{Total precipitation/Vapor influx}, \quad (8)$$

was estimated to be 35%. Similar values were found for Boxes B and C in Figure 8.

A curiosity in Table 2 (Row e) is that the total precipitation from the raw upslope model (equation 5) is very large, exceeding even the incoming vapor flux. This significant error points out that the processes neglected in the raw upslope model (i.e., airflow dynamics, cloud delays, and water vapor depletion) play essential limiting roles in the precipitation that occurs in the real atmosphere.

It is useful to test the linear theory (equation 6) on this well-documented event. Using the best available parameters, the linear theory was used to predict the precipitation field (Fig. 10), and this was compared against rain gauge data. The cloud-delay values were used as fitting parameters (Barstad and Smith, 2005).

As the conventional error measures, such as bias and root mean square error (RMSE), turned out to favor smooth fields, a more sensitive measure was proposed; the Location Sensitivity Skill (LSS). LSS is a measure of the RMSE skill degradation when the observing station locations are deliberately offset. Only if the skill degradation with station misplacement is significant, can we suppose that the predicted rainfall pattern has correct spatial detail. The results shown in Table 3 indicate that only cloud-delay values in the vicinity of  $\tau_c = \tau_r = 1000$  s give suitably low bias and RMSE and sufficiently high LSS. This estimate agrees with the estimates in section 4. Further details and other cases can be found in the original paper.

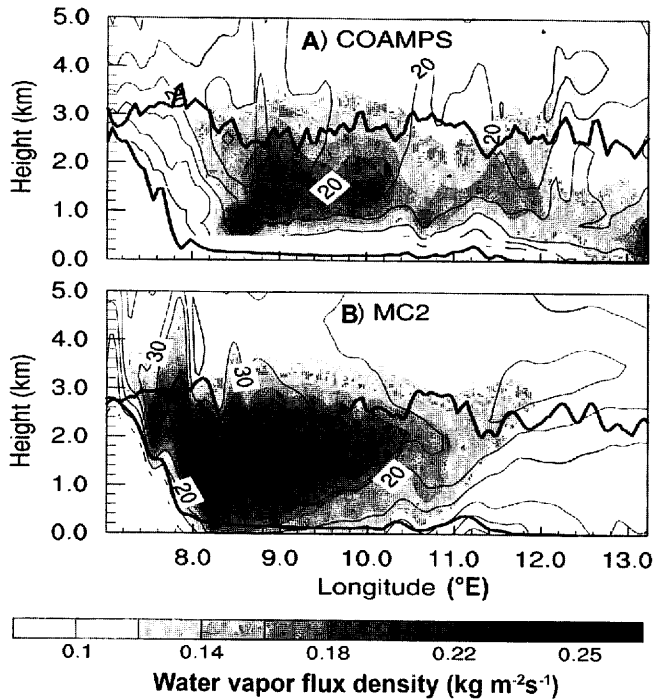


Figure 9. Incoming water vapor flux density (shaded,  $\text{kg m}^{-2}\text{s}^{-1}$ ) and northward wind speed (contoured,  $\text{m s}^{-1}$ ) through a vertical plane along  $45.5^\circ\text{N}$  at 08 UTC on 20 September 1999; (A) COAMPS, (B) MC2. Terrain in the plane of the cross section is shown, along with the projected crestline of the Alpine Massif. The area-integrated water vapor flux is given in Table 2 (Data are from Smith et al., 2003.)

TABLE 2. ALPINE WATER FLUXES, PRECIPITATION AND DRYING RATIOS FOR 20 SEPTEMBER 1999, DERIVED FROM FOUR MODELS

Row	Quantity	COAMPS	MC2	ECMWF forecast	ECMWF analysis
a	WV influx	56	53	42	44
b	WV outflux	33	35	33	29
c	Model precipitation	19	12	17	
d	Actual precipitation	19 (19)	19 (19)	19 (19)	19 (19)
e	Raw upslope precipitation	95	108		
f	DR%*(c/a)	34	23	40	
g	DR%*(d/a)	34	36	45	43

Note: Models and data are for Box A in Figure 8. Water vapor flux and precipitation values are accumulations over 24 h, in units  $10^{11}$  kg. The drying ratio (DR) is given in percent. The ECMWF analysis does not have precipitation. Actual precipitation values are independent estimates from the ETH (Frei and Haeller, 2001, personal commun.), and the University of Vienna (VERA in parentheses). Data are taken from Smith et al. (2003).

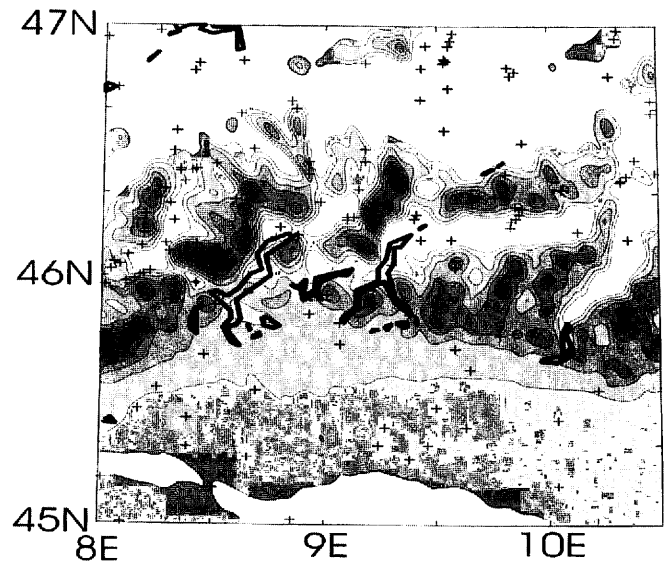


Figure 10. Hourly precipitation simulated by the linear model for 20 September 1999 in the Lago Maggiore area in northern Italy during Mesoscale Alpine Programme (MAP). Crosses indicate station locations. The contour interval is 2.5 mm/h. The Alpine terrain is not shown. (Data are from Barstad and Smith, 2005.)

TABLE 3. PRECIPITATION STATISTICS FOR 20 SEPTEMBER 1999 IN THE LAGO MAGGIORE AREA, COMPARING THE LINEAR MODEL AND RAIN-GAUGE DATA

$\tau$ (s)	Average (mm/h)	BIAS (mm/h)	RMSE (mm/h)	LSS <sub>RMSE</sub>
0	5.4	2.4	10.1	0.04
250	4.1	1.1	5.5	0.00
500	2.7	-0.3	3.7	0.03
750	2.5	-0.5	2.9	0.08
1000	2.6	-0.4	2.5	0.10
1500	2.8	-0.2	2.1	0.09
2000	2.7	-0.3	1.9	0.05
3000	2.3	-0.7	1.8	0.03
4000	1.9	-1.1	1.9	0.02

Note: The measures of goodness for the linear model changes as the characteristic time scale of conversion and fallout of hydrometeors ( $\tau$ ) increase. The observed mean of 77 stations is 3.0 mm/h (from Barstad and Smith, 2005). RMSE is root mean square error; LSS is Location Sensitivity Skill. BIAS is the average error.

It is useful to recall that southerly flow events, such as the one described above, cannot be extrapolated to understand longer-term climatology. In the Alps, winter northerly flow events and summertime convective events also contribute significantly to the annual average precipitation. In the next section, I consider a region with a narrower range of event types, so that individual events are more consistent with climatology.

## 6. OREGON CLIMATE GRADIENT

Another approach to the study of orographic precipitation uses average climatological precipitation distributions. For simplicity, I looked for a region where the annual averaged precipitation is composed of a number of fairly similar precipitation events. A reasonable choice for such a study is the coastal region of Oregon; well known for its strong west-to-east, wet-to-dry climate gradient (Bastash, 1998; Taylor and Hannan, 1999). The small variability from case to case is illustrated in Figure 11. This figure shows that the winds during precipitation events typically blow from the SW quadrant and with wind speeds exceeding 15 m/s. In fact, it seldom rains in western Oregon when the winds are easterly or northerly.

Another important characteristic of the region is that the rainfall is highly correlated with the atmospheric transport of water vapor across the coast (Fig. 12). Almost every pulse of vapor transport has a corresponding pulse of river discharge. This behavior is consistent with the hypothesis that forced ascent causes local precipitation.

Guided by Figures 11 and 12, the linear theory was computed for several representative environments and then averaged with weights corresponding to the frequency and duration of each event type. These climate precipitation fields can be compared

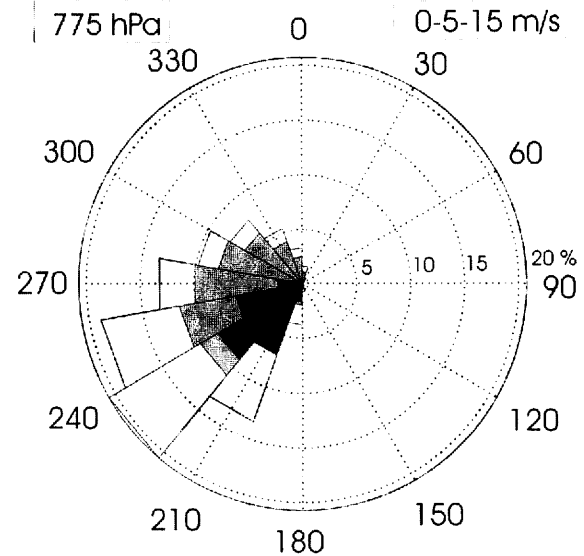


Figure 11. The 775 hPa statistical wind rose at a location near the Oregon coast (44°N, 124°W). Only wind conditions during precipitation are included. Data are from the ERA40 reanalysis for the period 1992–2002. Radial distance is the percent of time with wind direction in the sector. Shading indicates wind speeds greater than 5 and 15 m/s. (Data are from Smith et al., 2005.)

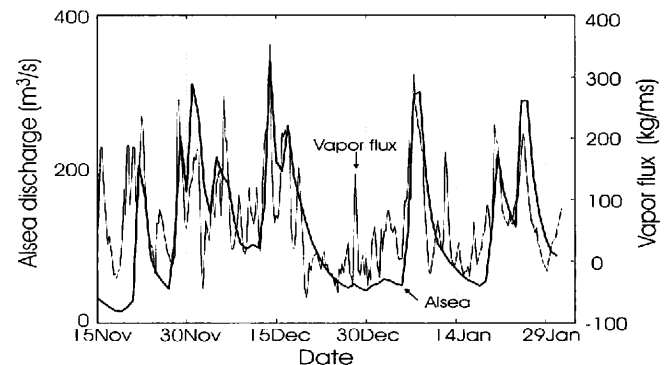


Figure 12. A time series of eastward vertically integrated water vapor flux density across the Oregon coast, computed from ERA40 data at the point 44°N, 124°W (light line: units  $\text{kg m}^{-1} \text{s}^{-1}$ ). The daily discharge from the Alsea River near Waldport is also shown (dark line: units  $\text{m}^3 \text{s}^{-1}$ ). The period is from 15 November 2001–31 January 2002, including the IMPROVE field project. Both records capture the strong event on 13–14 December 2001. (Data are from Smith et al., 2005.)

against the observed and interpolated annual fields from Daly et al. (1994). The results are shown in Figure 13. The PRISM (Precipitation-elevation Regression on Independent Slopes Model) interpolation scheme used by Daly is probably inaccurate on the smallest scales.

Figure 13 shows four fields related to the Oregon climate transition: the terrain, the annual averaged precipitation, the satellite-derived vegetation pattern, and the precipitation pattern



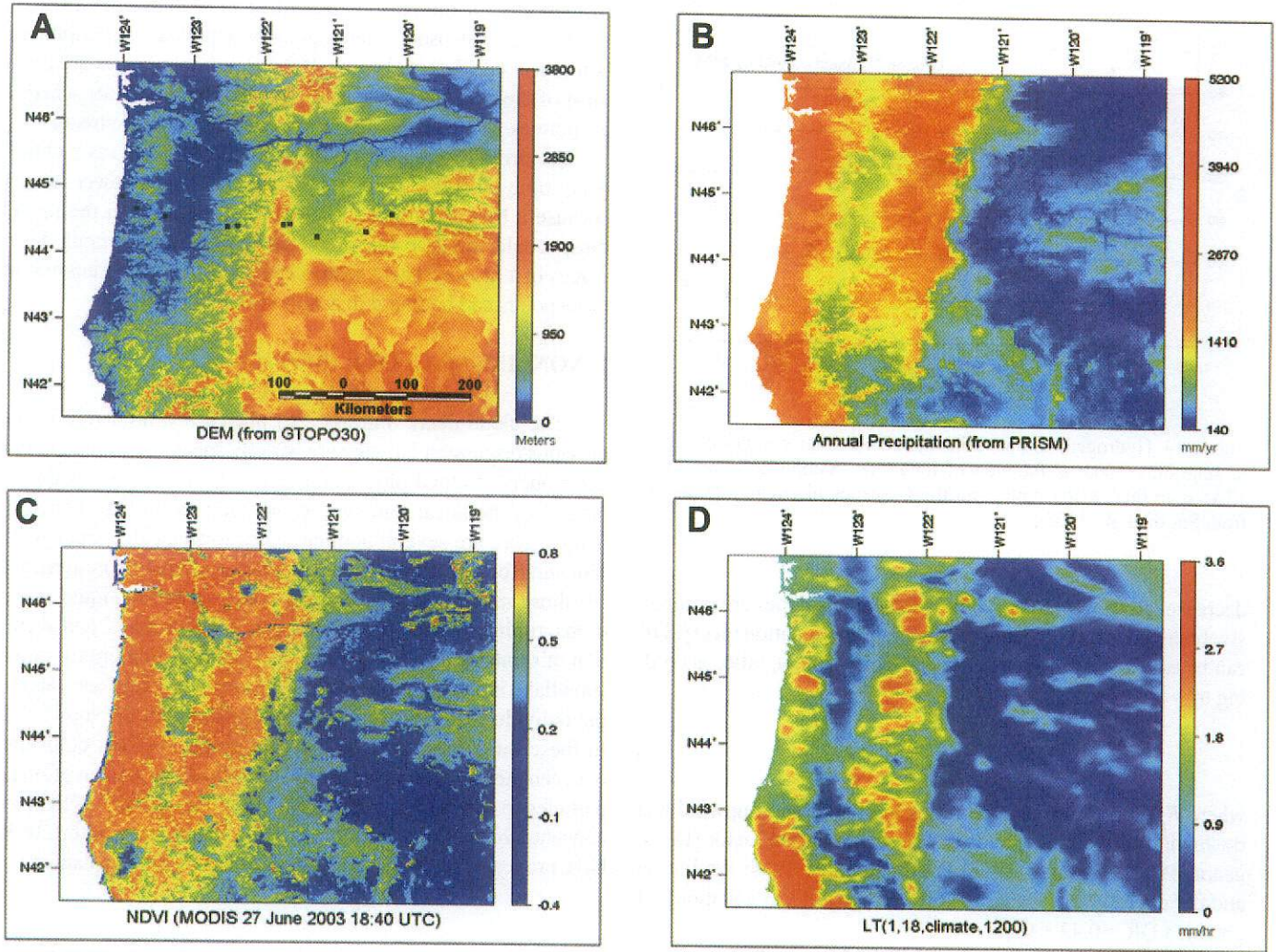


Figure 13. Four-part map of the Oregon climate transition. (A) Terrain elevation (with stream sample sites). (B) Annual precipitation (mm) using the PRISM (Precipitation-elevation Regression on Independent Slopes Model) interpolation algorithm. (C) Normalized difference vegetation index derived from MODIS (Moderate Resolution Imaging Spectroradiometer). (D) Precipitation rate from a linear theory climate run with  $P_{\infty} = 1 \text{ mm/h}$  and  $\tau = 1200 \text{ s}$ . Units are mm/h. All fields are shown with an enhanced pseudo-color scale. Blue indicates low values while red indicates high values. (Data are from Smith et al., 2005.)

derived from the linear model. Annual precipitation amounts are generally greater on the western (i.e., windward) slopes of the coastal and Cascade ranges. East of the Cascades, the precipitation is much reduced. The strong vegetation gradients generally reflect the availability of rainfall and soil moisture.

The model predicted field (Fig. 13D) is computed from equations 6 and 7, using a 1 km terrain map (Fig. 13A) and  $\tau_c = \tau_r = 1500 \text{ s}$ . It captures many of the features of the observed distributions. The terrain and the predicted precipitation fields contain a wide range of physical scales, and thus I found a variety of different balances. The smallest terrain scales (i.e., 1–5 km) have little impact on the precipitation fields, as their fields of forced ascent do not penetrate vertically and any condensate formed is evapo-

rated on the lee slopes before it can convert and precipitate. The intermediate scales (i.e., 5–30 km) produce hydrostatic airflow fields that penetrate to heights given by equation 2. The drift of condensate shifts the maximum precipitation point downstream so that it roughly coincides with the mountain peaks.

On the largest scales (i.e., 30–100 km), the drift is less important and the maximum precipitation occurs on the windward slopes. The strong rain shadow to the east of the Cascades is caused by evaporation in the descending air there.

To deduce optimum cloud-delay times ( $\tau_c$ ,  $\tau_r$ ) for Oregon climatology, I estimated the drying ratio (DR) using stable isotope ratios in dry-season, base-flow stream water samples. As shown in Figure 14, the relative concentration of deuterium to hydrogen



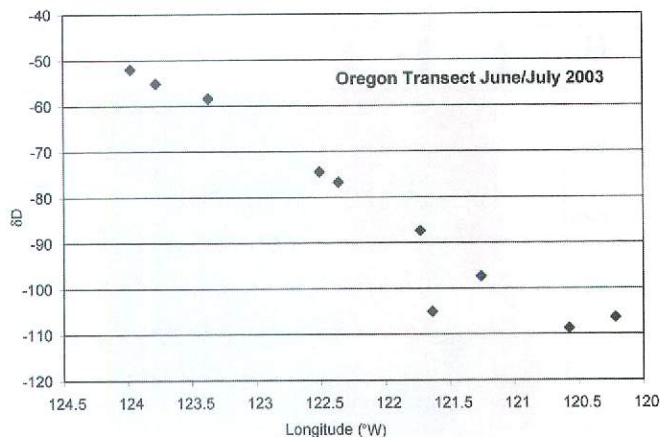


Figure 14. Hydrogen isotope ratios in stream-water samples collected in June–July 2003 as function of longitude. Sample locations (Fig. 13A) span the coastal range and the Cascades in Oregon. (Data are from Smith et al., 2005.)

decreases from west to east, because heavy isotopes are progressively rained out. According to Rayleigh fractionation theory, DR can be expressed in terms of the end-point isotope ratios according to

$$DR = 1 - (R_p/R_{p0})^{1/(\alpha-1)}, \quad (9)$$

where  $R_{p0}$  and  $R_p$  are isotope ratios in precipitation upwind and downwind of the range, and  $\alpha$  is the fractionation factor (Dansgaard, 1964; Friedman, 1953; Friedman et al., 1964; Warburton and deFelice, 1986). Using data from Figure 13 in equation 9, I obtained  $DR = 0.43 \pm 0.05$ .

The connection between cloud delay and drying ratio is shown in Figure 15. The steep decline in DR as cloud delay

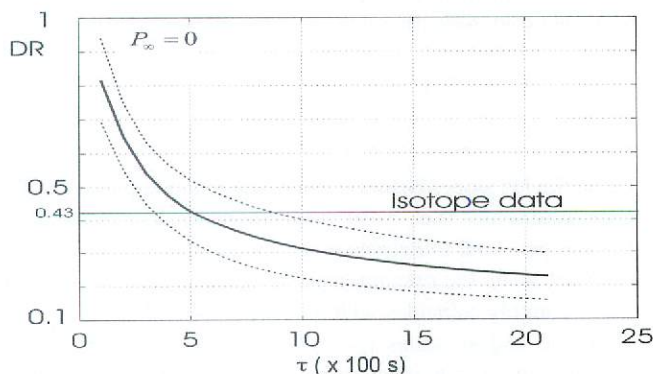


Figure 15. The drying ratio (DR) across western Oregon plotted against the cloud-delay time ( $\tau = \tau_c = \tau_p$ ) using the linear model under an ensemble of meteorological conditions. The background precipitation is set to zero for these runs. The mean DR and the  $1\sigma$  values are shown. The DR = 0.43 value from the stream-water isotope analysis is also indicated. (Data are from Smith et al., 2005.)

increases is for the reasons described in section 3. With small  $\tau = \tau_c = \tau_p$ , condensed water is quickly removed by precipitation before lee-side descent begins. If the cloud-delay times are large, most of the condensed water is advected to the lee side where it evaporates. Little total water is removed from the airstream.

According to Figure 15, the isotope data supports a cloud-delay time of 500 s or longer. I took 500 s as a lower bound, because a background precipitation, not included in the model runs, would increase the predicted drying ratio overall. Such values of  $\tau$  are consistent with section 4. A further discussion of these points can be found in Smith et al. (2005).

## 7. NONLINEAR CLOUD PHYSICS

The cloud-delay times ( $\tau_c$ ,  $\tau_p$ ) played a central role in the previous discussion but they are, strictly speaking, limited to linear models of cloud physics (equation 4). The  $\tau$  values are the inverse of the linear rate coefficients required in that model. In reality, there are several nonlinear processes inside clouds (e.g., Yau and Rogers, 1989). The most widely accepted nonlinearities are those associated with collision-coalescence of liquid water drops, riming of snow flakes by supercooled droplets, and accretion of small by large ice crystals. An example of a lightly rimed snowflake is shown in Figure 16. In this photograph, one can see the individual droplets that froze on impact with the snowflake. In these three processes, as the conversion involves collisions between the two types of particles, the rate of conversion of small particles to larger ones is proportional to the product of the two concentrations. To capture this process, Jiang and Smith (2003) have proposed the following system of steady-state equations

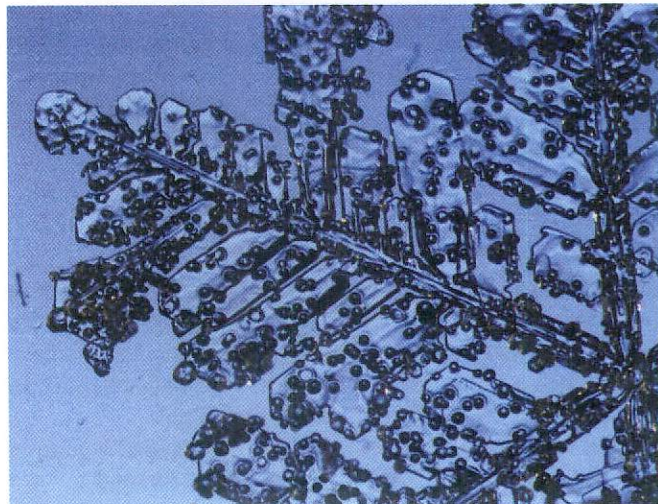


Figure 16. Photograph of a lightly rimed snowflake. The snowflake first formed by vapor deposition, then fell through a region with small supercooled liquid droplets. The droplets froze upon impact with the crystal. Horizontal scale is  $\sim 1$  mm. A typical cloud droplet size is  $\sim 20$   $\mu\text{m}$ . Photo by Ted Kinsman (sciencephotography.com).



$$\bar{U} \cdot \nabla q_c = S - \gamma q_c q_f, \quad (10a)$$

$$\bar{U} \cdot \nabla q_f = \lambda q_c q_f - q_f / \tau_f, \quad (10b)$$

As with equation 4, these equations describe the column densities of cloud particles ( $q_c$ ) and hydrometeors ( $q_f$ ). The cloud droplet equation (10a) has a source term  $S$ . The hydrometeor equation (10b) has a linear precipitation term in which the fallout time scale appears. These equations differ from equation 4 only in the form of the conversion term. In equation 10, the conversion has a quadratic form in which the product of the two concentrations appears, multiplied by a coefficient  $\gamma$ .

As these partial differential equations (10) are nonlinear, the solution method by Fourier transforms used in section 4 will not apply. Instead, we can remove the spatial variability by integrating horizontally over the volume of air lying above the windward slopes of the mountain (Fig. 17). I restrict my attention to ridge geometry, so that I needed only to integrate in the  $x$  direction to obtain average values.

$$Q = \frac{1}{a} \int_0^a q dx.$$

A similar procedure could be used with the linear equations (4); an exercise left to the reader. I assumed that no condensed water enters the box from upwind and that the advection out of the box (at the ridge line) is proportional to the wind speed ( $U$ ). When the nonlinear terms in equation 10 are averaged, new product terms arise of the form  $\langle q_c q_f \rangle$ , representing the correlations of cloud and hydrometeor density anomalies within the volume associated with convection, turbulence, or small-scale terrain.

Here I neglect these terms so the average condensate ( $Q_c, Q_f$ ), equations 10 become

$$0 = S - \gamma Q_c Q_f - (1/\tau_a) Q_c, \quad (11a)$$

$$0 = \gamma Q_c Q_f - (1/\tau_a + 1/\tau_f) Q_f, \quad (11b)$$

where  $S$  is now the volume averaged source. Integrating equation 5 gives  $S = \rho q_v U h_m / a$  ( $\text{kgm}^{-2}\text{s}^{-1}$ ).  $Q_c$  and  $Q_f$  are the averaged condensed water column densities ( $\text{kgm}^{-2}$ ), and  $\tau_a = a/U$  is the residence time for air in the test volume. Here,  $a$  is the width of the upslope region (Fig. 17).

While nonlinear equations usually require numerical solutions, these particular box-model equations (11) can be solved in closed form. For convenience, I first define a critical condensation rate

$$S_{\text{crit}} = \frac{\tau_a^{-1} + \tau_f^{-1}}{\gamma \tau_a}. \quad (12)$$

When  $S < S_{\text{crit}}$ , the physically relevant solution to equation 11 is  $Q_c = S \tau_a$  and  $Q_f = 0$ . This solution describes a state with condensed cloud water only, and with neither hydrometeors nor precipitation. The lenticular cloud in Figure 4 may be an example of this state. When  $S > S_{\text{crit}}$ ,

$$Q_c = S_{\text{crit}} \tau_a, \quad (13a)$$

and

$$Q_f = (S/S_{\text{crit}} - 1)/\gamma \tau_a. \quad (13b)$$

The average upslope precipitation rate is

$$P = Q_f \tau_f^{-1}, \quad (14)$$

so the precipitation efficiency (PE), assuming no lee-side precipitation, is

$$PE = P/S = (1 - S_{\text{crit}}/S)/(\tau_f/\tau_a + 1). \quad (15)$$

The threshold behavior in equation 13 and in Figure 18 is a bit of a surprise. The solution to equation 13 tells us that in order for the system to balance strong quadratic accretion-dominated conversion, the source function must be sufficiently strong. In other words, if the source of condensed water is too weak, accretion cannot be sustained. When  $S$  is far in excess of the critical value, equations 13 and 14 give

$$P = S/(\tau_f/\tau_a + 1). \quad (16)$$

Equation 16 describes a state with highly efficient conversion of cloud particles to hydrometeors. Hydrometeors are then partitioned between fallout and advection over the crestline, so called spillover. Only when fallout is fast compared to the residence time ( $\tau_f \ll \tau_a$ ) do we achieve the maximum possible upslope precipitation. Equation 16 then reduces to  $P = S$ .

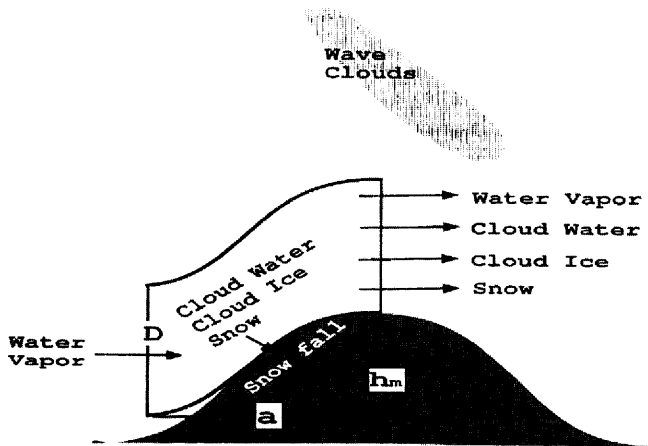


Figure 17. The box model described by equation 11, where  $a$  is mountain width and  $h_m$  is mountain height. Water vapor enters from the left and is partially condensed by the forced ascent. Condensed water is partitioned between precipitation on the windward slope and the advection of cloud water and hydrometeors over the ridge crest. (Data are from Jiang and Smith, 2003.)

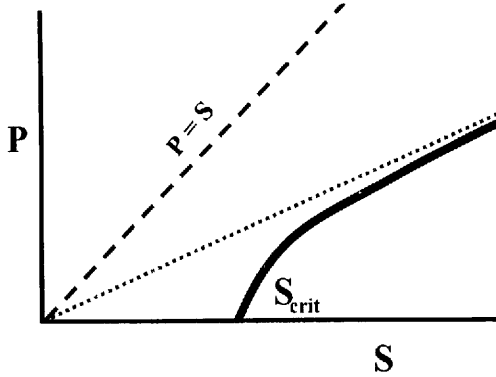


Figure 18. Solution to the nonlinear accretion-dominated box-model system (equation 11). The strength of the condensation source function ( $S$ ) is plotted against the upslope precipitation ( $P$ ). The solid curve is given by equations 13 and 14. The dotted curve is equation 15. The dashed curve ( $P = S$ ) represents perfect precipitation. (Theory is after Jiang and Smith, 2003.)

This cloud nonlinearity and threshold property does not necessarily invalidate the linear theory. In real clouds with many competing conversion pathways, abrupt threshold behavior is less likely to occur. Also lumped models, such as our two component representation of condensed water (equation 10), often exaggerate the abruptness of bifurcations. Furthermore, a background precipitation may already surpass the threshold, giving a more linear response to the terrain-forced perturbation. The nonlinear analysis is striking, however, and it suggests at least that the cloud-delay times may vary from case to case, depending on the average rate of water vapor condensation.

Nonlinearities in airflow dynamics and cloud physics can be more fully treated using numerical techniques. Existing community mesoscale models of moist airflow dynamics, run on fast computers, allow repeated simulation experiments to be carried out. To the extent that these models are valid, the runs can be used to determine the sensitivity of precipitation amount and pattern to physical and environmental parameters. Recent work by Colle (2004) investigated the influence of wind speed and shear, moist static stability, freezing level, and barrier height and width.

## 8. INFLUENCE OF PRECIPITATION ON EROSION AND LANDFORM EVOLUTION

The coupling of precipitation to erosion and landform evolution has been discussed recently by several authors (Burbank et al., 2003; Dadson et al., 2003; Reiners et al., 2003; Molnar, 2003). The idea is an intriguing one as it links processes acting over an enormous range of space and time scales. Millions of orographic precipitation events are needed to alter the terrain.

To motivate the following discussion, consider the shape of the Alpine Massif shown in Figure 8. Along the south side of the Alps, two concave indentations can be seen at latitude  $46^\circ\text{N}$ : one at  $9^\circ\text{E}$  and the other at  $13^\circ\text{E}$ . These two locations experience

especially high rainfall, perhaps because of the streams of water vapor that come from the Ligurian and Adriatic Seas or possibly because of the mountain shape itself. This coincidence of rainfall and terrain concavity allows us to speculate that atmospheric focusing of precipitation may have accelerated erosion, causing the terrain to evolve toward its current shape.

With a new scale-sensitive model of orographic precipitation at hand (equation 5), we are in a position to see how airflow dynamics and cloud physics might influence the patterns of erosion. To do this compactly, we must confine our treatment to a linear one-dimensional landscape evolution equation

$$dh(x)/dt = A\nabla^2 h(x) - BP(x) + T. \quad (17)$$

According to equation 17, terrain height evolves by diffusion (with coefficient  $A$ ), by erosion proportional to local precipitation (with coefficient  $B$ ), and by uniform tectonic uplift ( $T$ ). For simplicity, I considered a situation in which the background precipitation ( $P_\infty$ ) causes a uniform erosion that balances the regional uplift; so that  $BP_\infty = T$ . Subtracting this solution from equation 17 gives an evolution equation for the spatially varying part. The terrain evolution governed by equation 17 can be understood most easily by considering the slow changes occurring to a purely sinusoidal landform. Written in complex exponential form, it is:

$$h(x,t) = \text{Re} \left[ \hat{h} e^{i(kx + \omega t)} \right], \quad (18)$$

where  $\hat{h}$  is the amplitude,  $k (= 2\pi/\lambda)$  is the wavenumber (real), and  $\omega$  is the complex frequency. If  $\omega$  is real, the sine wave will maintain its amplitude but shift left or right. If  $\omega$  is imaginary, the terrain wave will grow or decay with time. If  $\omega$  is complex, the sine wave will change its amplitude and location as time passes. With equation 18, the perturbation part of equation 17 becomes

$$i\omega \hat{h} = -Ak^2 \hat{h} - B\hat{P}. \quad (19)$$

With  $\hat{P}$  given by equation 6, equation 19 gives

$$\omega = iAk^2 - \frac{BC_\infty \sigma}{[1 - imH_w][1 + i\sigma\tau_c][1 + i\sigma\tau_f]}. \quad (20)$$

According to equation 20, the diffusion and precipitation vectors can be added to determine the complex value of  $\omega$ . The interpretation of  $\omega$  as a vector in the complex plane will give insight into the coupling (Fig. 19). As expected, the diffusion vector is pure imaginary and points toward the decay field, thus acting to decay or smooth terrain irregularities. The raw upslope precipitation vector ( $H_w = \tau_c = \tau_f = 0$ ), with no gravity waves or cloud delays, points along the negative real axis. Thus, erosion acts to shift the evolving terrain downwind. This is true because the highest precipitation occurs on the steepest upwind slopes, so the erosion rates would be highest there. With weaker erosion on the lee slopes, the entire terrain pattern would move downwind.

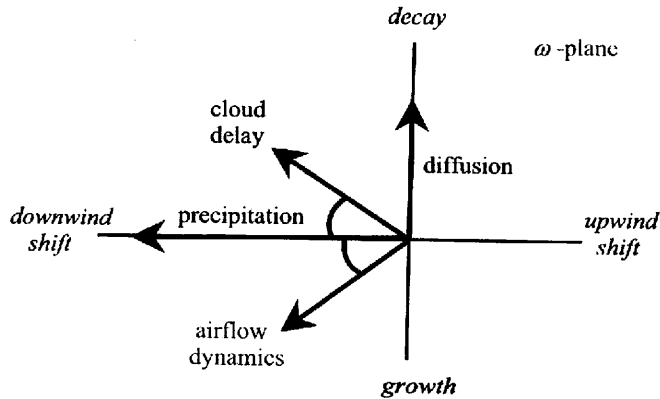


Figure 19. Phase diagram showing the complex  $\omega$  plane for erosion of a purely sinusoidal terrain. Real and imaginary parts of  $\omega$  represent the rates of terrain propagation and growth/decay. The pure diffusion vector corresponds to decay of the terrain. If there is a prevailing wind, the erosion due to precipitation causes the terrain to migrate downwind. Other aspects of precipitation physics, e.g., airflow dynamics or cloud physics, modify the erosion patterns slightly and may cause terrain growth or decay.

The effect of atmospheric gravity waves and cloud delays will shorten the precipitation vector in Figure 19 and rotate it. The influence of gravity waves is to rotate the precipitation vector clockwise. Acting alone, this will shift the precipitation further upwind so that erosion in the lower slopes would exceed erosion on the upper slopes and peaks. Terrain growth could occur under this scenario.

Cloud delays rotate the precipitation vector counterclockwise. This effect pushes the precipitation downwind toward the highest terrain. Erosion on the high peaks will decay the terrain.

Linear analysis (equation 20) is certainly oversimplified, and it may mislead us about the real world. It neglects nonlinear factors, such as stream-power erosion on slopes, that are thought to be of central importance in terrain evolution. It does serve to draw our attention to the importance of spatial phase shifts between terrain and precipitation and the fact that these shifts are scale dependent. These phase shifts may play a role in more realistic nonlinear models of terrain evolution.

## 9. CONCLUSIONS

In this brief review, I have focused on the physics of stable forced airflow lifting and precipitation caused by terrain. Meteorological disturbances such as fronts and cyclones usually play a key role in orographic precipitation by establishing a strong water vapor flux, high relative humidity, and background regional precipitation. Strong, moist airflows are able to rise over high terrain instead of being diverted around. The depth of penetration of the forced ascent, relative to the depth of the moist layer, determines the fraction of the vapor flux that can be condensed. The tilt of the airflow disturbance shifts the condensation pattern upwind. Even more important is the time required for hydrometeor formation

and fallout, relative to the transit time for air parcels over the terrain. These cloud delays control precipitation patterns, amount, and spillover. To clarify the physics, I have distinguished between linear and nonlinear processes.

Several other aspects deserve more attention than I can give here: cloud physics theory, observations and parameterizations, convective cloud dynamics, radar and satellite meteorology, and full numerical modeling and data initialization. Advances in these fields will not only help to improve short-term precipitation forecasting related to floods, avalanches, landslides, and water resources, but also teach us more about longer-term processes, such as glacier growth, terrain evolution, and regional climate change.

## ACKNOWLEDGMENTS

I very much appreciate the invitation to the GSA Penrose Conference in Taiwan in January 2003. The participants, with their enthusiastic questions and broad insights made the experience memorable. I appreciate discussion with N. Gasparini, Q. Jiang, J. Evans, and I. Barstad. Detailed suggestions by G. Roe and an anonymous reviewer improved the paper. Permission to use photographs by Jane English and Ted Kinsman is appreciated. This work is supported by National Science Foundation grant ATM-0112354 and National Aeronautics and Space Administration (NASA) grant NAG5-9316.

## REFERENCES CITED

- Asencio, N., Stein, J., Chong, M., and Gheusi, F., 2003, Analysis and simulation of local and regional conditions for the rainfall over the Lago Maggiore Target Area during MAP IOP2b: Quarterly Journal of the Royal Meteorological Society, v. 129, Part B, p. 565–586.
- Banta, R.M., 1990, The role of mountain flows in making clouds, in Blumen, W., ed., Atmospheric processes over complex terrain: Boston, Massachusetts, American Meteorological Society, Meteorological Monographs, v. 23, no. 45, p. 229–283.
- Banta, R.M., and Barker Schaaf, C., 1987, Thunderstorm genesis zones in the Colorado Rocky Mountains as determined by traceback of geosynchronous satellite images: Monthly Weather Review, v. 115, p. 463–476, doi: 10.1175/1520-0493(1987)115<0463:TGZITC>2.0.CO;2.
- Barcelon, A., and Fitzjarrald, D., 1985, A nonlinear steady model for moist hydrostatic mountain waves: Journal of Atmospheric Sciences, v. 42, p. 58–67, doi: 10.1175/1520-0469(1985)042<0058:ANSMFM>2.0.CO;2.
- Barros, A.P., and Lang, T.J., 2003, Monitoring the monsoon in the Himalayas: Observations in central Nepal, June 2001: Monthly Weather Review, v. 131, p. 1408–1427, doi: 10.1175/1520-0493(2003)131<1408:MTMITH>2.0.CO;2.
- Barros, A.P., and Lettenmaier, D.P., 1994, Dynamic modeling of orographically induced precipitation: Reviews of Geophysics, v. 32, no. 3, p. 265–284, doi: 10.1029/94RG00625.
- Barstad, I., and Smith, R.B., 2005, Evaluation of an orographic precipitation model: Journal of Hydrometeorology, v. 6, p. 85–99, doi: 10.1175/JHM-404.1.
- Bastash, R., 1998, Waters of Oregon: Corvallis, Oregon, Oregon State University Press, 278 p.
- Bousquet, O., and Smull, B.F., 2003, Observations and impacts of upstream blocking during a widespread orographic precipitation event: Quarterly Journal of the Royal Meteorological Society, v. 129, Part B, p. 391–409.
- Browning, K.A., Hill, F.F., and Pardoe, C.W., 1974, Structure and mechanism of precipitation and the effect of orography in a wintertime warm sector: Quarterly Journal of the Royal Meteorological Society, v. 100, no. 425, p. 555–562, doi: 10.1256/smsqj.42504.
- Burbank, D.W., Blythe, A.E., Putkonen, J., Pratt-Sitaula, B., Gabet, E.,

- Oskin, M., Barros, A., and Ojha, T.P., 2003, Decoupling of erosion and precipitation in the Himalayas: *Nature*, v. 426, no. 6967, p. 652–655, doi: 10.1038/nature02187 D. W.
- Buzzi, A., Tartaglione, N., and Malguzzi, P., 1998, Numerical simulations of the 1994 Piedmont flood: Role of orography and moist processes: *Monthly Weather Review*, v. 126, p. 2369–2383, doi: 10.1175/1520-0493(1998)126<2369:NSOTPF>2.0.CO;2.
- Colle, B.A., 2004, Sensitivity of orographic precipitation to changing ambient conditions and terrain geometries: An idealized modeling perspective: *Journal of Atmospheric Sciences*, v. 61, p. 588–606, doi: 10.1175/1520-0469(2004)061<0588:SOOPTC>2.0.CO;2.
- Collier, C.G., 1975, A representation of the effects of topography on surface rainfall within moving baroclinic disturbances: *Quarterly Journal of the Royal Meteorological Society*, v. 101, p. 407–422, doi: 10.1256/smsqj.42901.
- Dadson, S.J., Hovius, N., and Chen, H.G., 2003, Links between erosion, runoff variability and seismicity in the Taiwan orogen: *Nature*, v. 426, no. 6967, p. 648–651, doi: 10.1038/nature02150.
- Daly, C., Neilson, R.P., and Phillips, D.L., 1994, A statistical-topographic model for mapping climatological precipitation over mountainous terrain: *Journal of Applied Meteorology*, v. 33, p. 140–158, doi: 10.1175/1520-0450(1994)033<0140:ASTMFM>2.0.CO;2.
- Dansgaard, W., 1964, Stable isotopes in precipitation: *Tellus*, v. 16, p. 436–468.
- Doyle, J., and Smith, R.B., 2003, Mountain waves over the Hohe Tauern: Influence of upstream diabatic effects: *Quarterly Journal of the Royal Meteorological Society*, v. 129, no. 588, p. 799–823, doi: 10.1256/qj.01.205.
- Durrán, D.R., and Klemp, J.B., 1982, The effects of moisture on trapped mountain lee waves: *Journal of Atmospheric Sciences*, v. 39, p. 2490–2506, doi: 10.1175/1520-0469(1982)039<2490:TEOMOT>2.0.CO;2.
- Evans, J., Smith, R.B., and Oglesby, R., 2004, Middle East climate simulation and dominant precipitation processes: *International Journal of Climatology*, v. 24, p. 1671–1694, doi: 10.1002/joc.1084.
- Fraser, A.B., Easter, R.C., and Hobbs, P.V., 1973, A theoretical study of the flow of air and fallout of solid precipitation over mountainous terrain: Part I. Airflow model: *Journal of Atmospheric Sciences*, v. 30, p. 801–812, doi: 10.1175/1520-0469(1973)030<0801:ATSOTF>2.0.CO;2.
- Friedman, I., 1953, Deuterium content of natural waters and other substances: *Geochimica et Cosmochimica Acta*, v. 4, p. 89–103, doi: 10.1016/0016-7037(53)90066-0.
- Friedman, I., Redfield, A.C., Schoen, B., and Harris, J., 1964, The variation of the deuterium content of natural waters in the hydrologic cycle: *Reviews of Geophysics*, v. 2, p. 177–223.
- Georgis, J.-F., Roux, F., Chong, M., and Pradier, S., 2003, Triple-Doppler radar analysis of the heavy rain event observed in the Lago Maggiore region during MAP IOP 2b: *Quarterly Journal of the Royal Meteorological Society*, v. 129, Part B, p. 495–522.
- Hobbs, P.V., Easter, R.C., and Fraser, A.B., 1973, A theoretical study of the flow of air and fallout of solid precipitation over mountainous terrain: Part II. Microphysics: *Journal of Atmospheric Sciences*, v. 30, p. 813–823, doi: 10.1175/1520-0469(1973)030<0813:ATSOTF>2.0.CO;2.
- Jiang, Q., 2003, Moist dynamics and orographic precipitation: *Tellus*, v. 55A, p. 301–316.
- Jiang, Q., and Smith, R.B., 2003, Cloud timescale and orographic precipitation: *Journal of Atmospheric Sciences*, v. 60, p. 1543–1559, doi: 10.1175/2003.1.
- Lin, Y.-L., Han, J., Hamilton, D.W., and Huang, C.-Y., 1999, Orographic influence on a drifting cyclone: *Journal of Atmospheric Sciences*, v. 56, p. 534–562, doi: 10.1175/1520-0469(1999)056<0534:OIOADC>2.0.CO;2.
- Medina, S., and Houze, R.A., 2003, Air motions and precipitation growth in Alpine storms: *Quarterly Journal of the Royal Meteorological Society*, v. 129, Part B, p. 345–371.
- Molnar, P., 2003, Geomorphology—Nature, nurture and landscape: *Nature*, v. 426, no. 6967, p. 612–614, doi: 10.1038/426612a.
- Passarelli, R.E., and Boehme, H., 1983, The orographic modulation of pre-warm-front precipitation in southern New England: *Monthly Weather Review*, v. 111, p. 1062–1070, doi: 10.1175/1520-0493(1983)111<1062:TOMOPW>2.0.CO;2.
- Rauber, R.M., and Grant, L.O., 1986, The characteristics and distribution of cloud water over the mountains of northern Colorado during wintertime storms. Part II: Spatial distribution and microphysical characteristics: *Journal of Applied Meteorology*, v. 25, p. 489–504, doi: 10.1175/1520-0450(1986)025<0489:TCADOC>2.0.CO;2.
- Raymond, D.J., and Wilkening, M.H., 1982, Flow and mixing in New Mexico mountain cumuli: *Journal of Atmospheric Sciences*, v. 39, p. 2211–2228, doi: 10.1175/1520-0469(1982)039<2211:FAMINM>2.0.CO;2.
- Reiners, P.W., Ehlers, T.A., Mitchell, S.G., and Montgomery, D.R., 2003, Coupled spatial variations in precipitation and long-term erosion rates across the Washington Cascades: *Nature*, v. 426, no. 6967, p. 645–647, doi: 10.1038/nature02111.
- Rotunno, R., and Ferretti, R., 2003, Orographic effects on rainfall in MAP cases IOP2b and IOP8: *Quarterly Journal of the Royal Meteorological Society*, v. 129, Part B, p. 373–390.
- Smith, R.B., 1979, The influence of mountains on the atmosphere: *Advances in Geophysics*, v. 21, p. 87–230.
- Smith, R.B., 1980, Linear theory of stratified hydrostatic flow past an isolated mountain: *Tellus*, v. 32, p. 348–364.
- Smith, R.B., 2003, A linear time-delay model of orographic precipitation: *Journal of Hydrology*, v. 282, p. 2–9, doi: 10.1016/S0022-1694(03)00248-8.
- Smith, R.B., and Barstad, I., 2004, A linear theory of orographic precipitation: *Journal of Atmospheric Sciences*, v. 61, p. 1377–1391, doi: 10.1175/1520-0469(2004)061<1377:ALTOOP>2.0.CO;2.
- Smith, R.B., Jiang, Q.F., Fearon, M.G., Tabary, P., Dorninger, M., Doyle, J.D., and Benoit, R., 2003, Orographic precipitation and air mass transformation: An alpine example: *Quarterly Journal of the Royal Meteorological Society*, v. 9, Part B, p. 433–454.
- Smith, R.B., Barstad, I., and Bonneau, L., 2005, Orographic precipitation and Oregon's climate transition: *Journal of Atmospheric Sciences*, v. 62, p. 177–191, doi: 10.1175/JAS-3376.1.
- Taylor, G.H., and Hannan, C., 1999, *The climate of Oregon: Corvallis, Oregon*. Oregon State University Press, 211 p.
- Uttal, T., Rauber, R.M., and Grant, L.O., 1988, Distributions of liquid, vapor, and ice in an orographic cloud from field observations: *Journal of Atmospheric Sciences*, v. 45, no. 7, p. 1110–1122, doi: 10.1175/1520-0469(1988)045<1110:DOLVAL>2.0.CO;2.
- Wallace, J.M., and Hobbs, P.V., 1977, *Atmospheric science: An introductory survey*. New York, Academic Press, 467 p.
- Wang, J.-J., Rauber, R.M., Ochs, H.T., and Carbone, R.E., 2000, The effects of the island of Hawaii on offshore rainband evolution: *Monthly Weather Review*, v. 128, p. 1052–1069, doi: 10.1175/1520-0493(2000)128<1052:TEOTIO>2.0.CO;2.
- Warburton, J.A., and deFelice, T.P., 1986, Oxygen isotopic composition of central Sierra Nevada precipitation: Part I: Identification of ice-phase water capture regions in winter storms: *Atmospheric Research*, v. 20, p. 11–22, doi: 10.1016/0169-8095(86)90004-9.
- Wratt, D.S., Ridley, R.N., Sinclair, M.R., Larsen, H., Thompson, S.M., Henderson, R., Austin, G.L., Bradley, S.G., Auer, A., Sturman, A.P., Owens, I., Fitzharris, B., Ryan, B.F., and Gayet, J.-F., 1996, The New Zealand Southern Alps experiment: *Bulletin of the American Meteorological Society*, v. 77, p. 683–692, doi: 10.1175/1520-0477(1996)077<0683:TNZSAE>2.0.CO;2.
- Wurtele, M.G., Sharman, R.D., and Datta, A., 1996, Atmospheric lee waves: *Annual Review of Fluid Mechanics*, v. 28, p. 429–476, doi: 10.1146/annurev.fl.28.010196.002241.
- Yau, M.K., and Rogers, R.R., 1989, *Short course in cloud physics* (3rd edition): Butterworth-Heinemann, 304 p.
- Yuter, S.E., and Houze, R.A., 2003, Microphysical modes of precipitation growth determined by S-band vertically pointing radar in orographic precipitation during MAP: *Quarterly Journal of the Royal Meteorological Society*, v. 129, Part B, p. 455–476.

MANUSCRIPT ACCEPTED BY THE SOCIETY 23 JUNE 2005